Geophys. J. Int. (2011) **184,** 1327–1340 doi: 10.1111/j.1365-246X.2010.04909.x

Fast and accurate 3-D ray tracing using bilinear traveltime interpolation and the wave front group marching

Jianzhong Zhang,[1,2] Yueqin Huang,[2,4] Lin-Ping Song[3] and Qing-Huo Liu[4]

[1] *College of Marine Geoscience, Ocean University of China, Qingdao* 266100*, China. E-mail: zhangjz@ouc.edu.cn*
[2] *School of Information Science and Technology, Xiamen University, Xiamen* 361005*, China*
[3] *Department of Earth and Ocean Sciences, University of British Columbia, Canada*
[4] *Department of Electrical and Computer Engineering, Duke University, Durham, NC* 27705*, USA*

Accepted 2010 November 30. Received 2010 November 29; in original form 2010 January 22

SUMMARY

We propose a new ray tracing technique in a 3-D heterogeneous isotropic media based on bilinear traveltime interpolation and the wave front group marching. In this technique, the media is discretized into a series of rectangular cells. There are two steps to be carried out: one is a forward step where wave front expansion is evolved from sources to whole computational domain and the subsequent one is a backward step where ray paths are calculated for any source–receiver configuration as desired. In the forward step, we derive a closed-form expression to calculate traveltime at an arbitrary point in a cell using a bilinear interpolation of the known traveltimes on the cell's surface. Then the group marching method (GMM), a fast wave front advancing method, is applied to expand the wave front from the source to all girds. In the backward step, ray paths starting from receivers are traced by finding the intersection points of potential ray propagation vectors with the surfaces of relevant cells. In this step, the same TI scheme is used to compute the candidate intersection points on all surfaces of each relevant cell. In this process, the point with the minimum traveltime is selected as a ray point from which the similar step is continued until sources. A number of numerical experiments demonstrate that our 3-D ray tracing technique is able to achieve very accurate computation of traveltimes and ray paths and meanwhile take much less computer time in comparison with the existing popular ones like the finite-difference-based GMM method, which is combined with the maximum gradient ray tracing, and the shortest path method.

Key words: Numerical solutions; Body waves; Computational seismology; Wave propagation.

1 INTRODUCTION

Seismic rays are a good approximation to wave propagation under high-frequency regime (Spudich & Neil 1984; Cerveny 2001; Grunberg *et al.* 2002). As compared to a full wave solution, they are able to provide a simple yet effective means to formulate and conduct practical seismic imaging problems such as tomography and migration (Vasco & Majer 1993; Giudici & Gualteri 1998; Cardarelli & Cerreto 2002; Majdanski *et al.* 2005) that are widely used in oil exploration, recovery, engineering, and study of the Earth's interior. The computation of seismic rays is an important integral part in these applications and has been an active topic in seismic community. Since Julian and Gubbin's classical study (1977), many attempts have been made to improve ray tracing performance (e.g. Hturber & Ellsworth 1980; Moser 1991; Asakawa & Kawanaka 1993; Fischer & Lees 1993; Klimes & Kvasnicka 1994; Wang & Houseman 1995; Van *et al.* 2001; Zhang *et al.* 2004; Zhao *et al.* 2004; Zhou *et al.* 2004; Bai *et al.* 2007). In spite of these developments, the ray tracing in 3-D media has been remaining a major issue in terms of computational accuracy and speed. Towards the goal of a fast computation in 3-D media without compromising accuracy, we propose a bilinear traveltime interpolation scheme for 3-D media and formulate a hybrid ray tracing approach by combining the wave front group marching method (Kim 2002). An extensive overview of ray tracing literature is not the scope of the paper. Instead, we will go through the most relevant references to our work.

Traditional ray tracing may be categorized into shooting and bending methods. In shooting methods, ray tracing is conducted by solving the first-order ray differential equations given a family of initial take-off angles emitted from a source location. The approximation solution of ray differential equations is often obtained by an iterative process. That is an initial value problem. In bending methods, rays are sought by solving a minimization problem requested by Fermat's principle given source and receiver locations. That is a boundary problem. Both

classical ray tracing methods encounter convergence problems in a complicated medium, for example, either converging slowly or being easily trapped into a local minimum.

Subsequently, some other approaches were proposed like the eikonal equation solution methods (Vidale 1988, 1990; Qin *et al.* 1992) and the shortest path method (SPM) (Moser 1991; Klimes & Kvasnicka 1994) to overcome the problem met in the traditional ray tracing methods.

The idea of the SPM was originated in network theory (Dijkstra 1959) in which grids are distributed and a shortest distance route is sought from a starting grid by continuously selecting a second 'starting' gird with a minimum distance from all neighbours. Nakanishi and Yamaguchi (1986) introduced this method in the inversion of 2-D mantle velocity structure. Moser (1991) systematically investigated the SPM in the context of seismic ray tracing. Since that, the SPM has been one of widely used ray tracing tools in 3-D media. Compared to the traditional methods, the SPM always guarantees a global convergence to find ray paths satisfying the minimum traveltime principle in an arbitrary medium. Its implementation is simple. To achieve the balance between the accuracy and computational time in the SPM, the improved versions of the SPM were proposed by Klimes and Kvasnicka (1994) and Zhao *et al.* (2004) and Bai *et al.* (2007). In Klimes and Kvasnicka (1994), they used a regular network that can achieve a run-time at least five times faster than Moser's method (1991) for 3-D cases. In Zhao *et al.* (2004) and Bai *et al.* (2007), the authors designed an irregular network SPM algorithm and demonstrated that their approach required much less memory and saved significant amount of CPU time in contrast to Klimes and Kvasnicka's scheme (1994). Furthermore, Van Avendonk *et al.* (2001) proposed a ray tracing technique by combining the bending method and the SPM to improve accuracy of traveltime computation.

In the eikonal equation-based solution methods, the eikonal equation is solved by finite-difference (FD) scheme and wave front expansion is evolved. The ray path between a pair of source and receiver can be traced back by finding the maximum gradient of computed wave fronts (Vidale 1988; Podvin *et al.* 1991). To advance wave fronts in the FD method, the fast marching method (FMM) (Sethian *et al.* 1999, 2001; Rawlinson *et al.* 2004) might be used. The FMM uses the narrow band technique and requires sorting the solution at each step of the narrow band. Its computational cost is $O(N \log N)$, where N is the total number of grid nodes in the computational domain. Kim (2002) introduced an optimal variant of FMM called the group marching method (GMM), in which the condition of causality must be held when expanding wave fronts. The GMM advances a group of gridpoints once at a time, rather than sorting solutions in the narrow band to march forward a single gridpoint as in the FMM, thus it costs only $O(N)$. Both FMM and GMM are unconditionally stable. Another kind of eikonal equations solver called the fast sweeping method (FSM) uses the WENO scheme for wave front calculation. Hysing *et al.* (2005) provided an overview of algorithm performance for FMM and FSM methods and concluded that the FMM outperforms all other methods with respect to speed, accuracy and robustness. That's an important reason why we choose GMM, the optimal variance of FMM, for comparison in the numerical experiments.

Besides, Asakawa and Kawanaka (1993) proposed a 2-D ray tracing method using linear traveltimes interpolation (LTI). The LTI-based traveltime computation has some similarity to the FD solution of the eikonal (Vidale 1988) but is more accurate (Asakawa *et al.* 1993). Later still in 2-D cases, some work was attempted to improve the LTI method (Li *et al.* 1993; Cardarelli *et al.* 2002; Vanelle *et al.* 2002; Zhou *et al.* 2004). Extending the LTI method to 3-D media seems difficult probably because in 3-D cells the extremum solution of LTI functions governed by Fermat's principle has no closed-form expression as in 2-D problems, while the computation of a numerical solution can be time-consuming and is not desirable.

In light of advantages of LTI method shown in 2-D cases, we would generalize the idea of LTI to 3-D media. To our knowledge, this is the first attempt to do so. In brief, we are able to derive the equations to analytically calculate traveltime between any two points in a cell using our bilinear interpolation scheme over 3-D grids. In the continuation step, the GMM is used to quickly march and locate wave front. In the sequel traveltimes and wave fronts are updated continuously. Incorporating the unconditionally stable GMM method for wave front expansion is different from the traditional 2-D LTI scheme which may violate causality of wave propagation. Once all traveltimes and wave fronts are determined, ray paths can be found by tracing from the receivers through relevant cells back to the sources. That is our 3-D ray tracing approach formed by combining the features of the traveltime interpolation and the wave front group marching. Note that in the backward process of ray tracing, the intersection points between ray paths and related cells' surfaces are sought analytically and accurately using the traveltime interpolation-based equations without calculating maximum gradient of wave fronts as in the FD-based FMM/GMM methods. Additionally, the 3-D LTI has a potential advantage of more easily to be accomplished for models with irregular cell discretization. The extension of this ray tracing technique to irregular cells has been conducted recently (Huang *et al.* 2010).

2 METHOD

2.1 Bilinear interpolation and traveltime calculation

Let Δx, Δy and Δz be the cell lengths in x, y and z directions, respectively. Consider each cell with a uniform/average velocity of v. Then the ray path in each cell is a straight line. The first step is to compute traveltime between two points under known conditions. This problem can be dealt with four cases.

Case (1). In Fig. 1(a), suppose that traveltimes at four grid nodes A, B, C and D on the left surface of a cell have been computed. Our problem is to find a point S on the left surface so that the traveltime from S to E is a minimum. Assume that S is located at (x_S, y_S, z_S). The

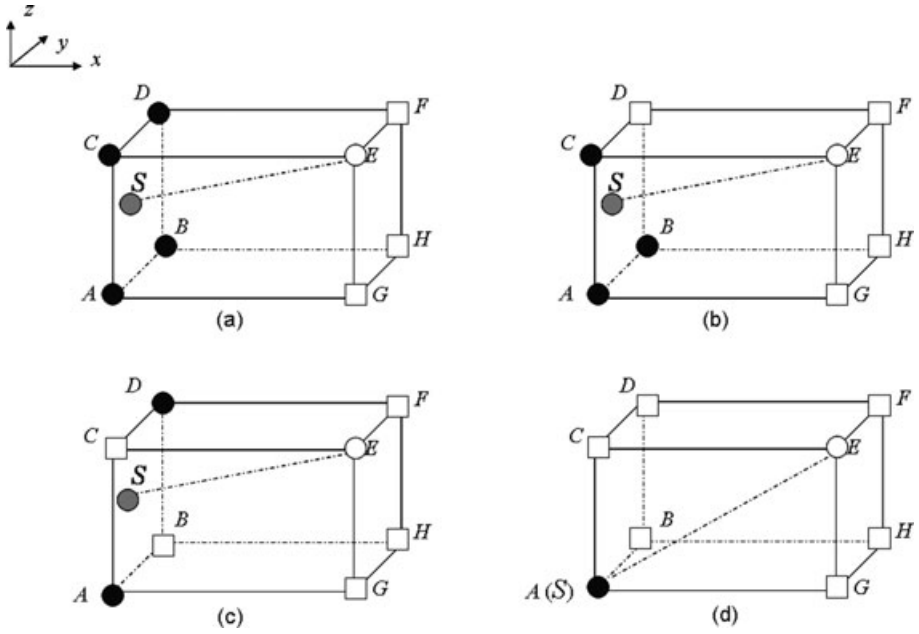

Figure 1. Diagrams show fours cases to calculate traveltime from nodes S (grey circle) to E (open circle) using the known traveltimes at nodes or node (solid circle) (a) A, B, C and D; (b) A, B and C; (c) A and B; (d) A only. Small squares denote nodes whose traveltimes are unknown.

coordinates for A, B, C and D are denoted as (x_S, y_1, z_1), (x_S, y_2, z_1), (x_S, y_1, z_2) and (x_S, y_2, z_2), respectively, with their corresponding traveltime of t_1, t_2, t_3 and t_4. Define $y_0 = (y_1 + y_2)/2$, $z_0 = (z_1 + z_2)/2$ as the centre of the left surface (y–z plane in this example).

One might calculate traveltime between points S and E using the FD solution of the 3-D eikonal equation. Here, we propose new equations to calculate 3-D traveltimes based on bilinear traveltime interpolation (TI). The later tests show that our scheme is able to provide much accurate solution than the FD scheme (Vidale 1988, 1990) when a computational domain is subdivided into a number of big cells.

Assume that traveltime varies linearly with distance in any direction on a surface of one cell. The traveltime at S can be expressed by a bilinear interpolation function of traveltimes on the four vertexes of the surface (Fig. 1a)

$$t_S = ag + bh + cgh + d, \tag{1}$$

where $g = y_S - y_0$, $h = z_S - z_0$, $a = (t_2 - t_1 + t_4 - t_3)/(2\Delta y)$, $b = (t_1 - t_3 + t_2 - t_4)/(2\Delta z)$, $c = (t_2 - t_1 - t_4 + t_3)/(\Delta y \Delta z)$ and $d = (t_1 + t_2 + t_3 + t_4)/4$. The traveltime from S to E can be written as

$$t_E = t_S + \sqrt{(x_E - x_S)^2 + (y_E - y_0 - g)^2 + (z_E - z_0 - h)^2}/v. \tag{2}$$

To derive an analytical solution, we approximate the second term in eq. (2) by using Taylor expansion about the point (y_0, z_0) to second-order accuracy for a function that depends on two variables. Eq. (2) then is approximated by the expression in (3),

$$\begin{aligned} t_E = t_S + \big\{ & A - g(y_E - y_0)/A - h(z_E - z_0)/A + 0.5\left[g^2/A - g^2(y_E - y_0)^2/A^3\right] \\ & + 0.5\left[h^2/A - h^2(z_E - z_0)^2/A^3\right] + gh(y_E - y_0)(z_0 - z_E)/A^3\big\}/v, \end{aligned} \tag{3}$$

where $A = \sqrt{(x_E - x_S)^2 + (y_E - y_0)^2 + (z_E - z_0)^2}$.

Substitute t_S in eq. (1) into eq. (3) and according to the Fermat principle set the derivatives of t_E with respect to the coordinates g and h equal to zeros

$$\begin{cases} \partial t_E/\partial g = 0 \\ \partial t_E/\partial h = 0. \end{cases} \tag{4}$$

The expressions of eq. (4) are tedious and thus omitted. After some manipulation, we then obtain the solutions of g and h as follows

$$g = \frac{A^2\left\{(bvA + z_0 - z_E)\left[cvA^3 - (y_0 - y_E)(z_0 - z_E)\right] - 2(avA + y_0 - y_E)\left[A^2 - (z_0 - z_E)^2\right]\right\}}{4\left[A^2 - (y_0 - y_E)^2\right]\left[A^2 - (z_0 - z_E)^2\right] - \left[cvA^3 - (y_0 - y_E)(z_0 - z_E)\right]^2} \tag{5}$$

$$h = \frac{A^2\left\{(avA + y_0 - y_E)\left[cvA^3 - (y_0 - y_E)(z_0 - z_E)\right] - 2(bvA + z_0 - z_E)\left[A^2 - (y_0 - y_E)^2\right]\right\}}{4\left[A^2 - (y_0 - y_E)^2\right]\left[A^2 - (z_0 - z_E)^2\right] - \left[cvA^3 - (y_0 - y_E)(z_0 - z_E)\right]^2}, \tag{6}$$

where g and h determine the position of point S on the left surface of the cell in Fig. 1(a), from which the wave propagates to the point E. After calculating g and h with eqs (5) and (6), the traveltime from S to E can be computed with eq. (2). Recalling the definition of g and h with respect to the centre of a surface of one cell, we obtain the range of g and h within $-0.5\Delta y \le g \le 0.5\Delta y$, $-0.5\Delta z \le h \le 0.5\Delta z$, respectively.

Case (2). In this case, we have known traveltimes at three grid nodes A, B and C (Fig. 1b), denoted as t_1, t_2 and t_3, respectively. Using the linear interpolation function, the traveltime at S can be expressed as

$$t_S = t_1 + (t_2 - t_1)(y_S - y_1)/\Delta y + (t_3 - t_1)(z_S - z_1)/\Delta z \tag{7}$$

and then the traveltime from S to E can be written as

$$t_E = t_S + \sqrt{(x_E - x_S)^2 + (y_E - y_S)^2 + (z_E - z_S)^2}/v. \tag{8}$$

Similar to the derivation of eqs (5) and (6), the Fermat principle requires the derivations of with respect to y_s and z_s equal to zeros. In this case the analytic solutions can be derived without any approximation and are listed as follows:

$$y_S = y_E \pm \frac{\Delta z(t_2 - t_1)(x_E - x_0)}{\sqrt{(\Delta y \Delta z/v)^2 - [\Delta y(t_3 - t_1)]^2 - [\Delta z(t_2 - t_1)]^2}} \tag{9}$$

$$z_S = z_E \pm \frac{\Delta y(t_3 - t_1)(x_E - x_0)}{\sqrt{(\Delta y \Delta z/v)^2 - [\Delta y(t_3 - t_1)]^2 - [\Delta z(t_2 - t_1)]^2}}, \tag{10}$$

where the operator $\pm$ should be determined by the boundary conditions $y_1 \le y_S \le y_2$ and $z_1 \le z_S \le z_2$. For example, when the fractional term (denoted as f_y) in eq. (9) satisfies $y_1 - y_E \le f_y \le y_2 - y_E$, $+$ is used and $-$ is used when $y_E - y_1 \ge f_y \ge y_E - y_2$. The same sign rule is applied to eq. (10). With the known coordinates of point S, the traveltime from S to E can be computed with eq. (8). In particular, there may be several (y_s, z_s) solutions satisfied with the boundary conditions, the one with a minimum value of t_E is selected.

Case (3). When known traveltimes are available only at two grid nodes (Fig. 1c), this is equivalent to a 2-D case. The solutions given by Asakawa and Kawanaka (1993) and Zhang *et al.* (2004) require that the two known nodes should be located parallel to an axis in the Cartesian coordinate system. For completeness, we give the equations for cases when the two nodes are located diagonally as (here we suppose traveltimes at A and D have been known)

$$t_E = t_1 + \hat{y}\frac{t_2 - t_1}{\Delta y} + \sqrt{(x_E - x_{S'}) + (y_E - y_1 - \hat{y})^2 + (z_E - z_1)^2}/v, \tag{11}$$

where

$$\hat{y} = y_E - y_1 + \sqrt{\frac{(t_2 - t_1)^2[(x_E - x_{S'})^2 + (z_E - z_1)^2]}{(\Delta y/v)^2 - (t_2 - t_1)^2}}. \tag{12}$$

Formulas (11) and (12) are an extension of the existing 2-D LTI scheme.

Case (4). This is the simplest case where the traveltime is known at one node (here we suppose traveltime at point A has been known). In this case, point A is deemed as point S, and the traveltime between points S and E is the product of the reciprocal of velocity of the cell and their Euclidean distance (Fig. 1d).

This completes the description of our bilinear interpolation schemes to compute traveltimes in 3-D discretized cells. Note that in a rectangular cell, the traveltime at a candidate point (e.g. point E in the above) should be computed separately with respect to each surface where one or more known grid nodes exist. The minimum of those calculated traveltimes at that point will be selected as its wave front traveltime.

2.2 Accuracy check

There is a question if the solution derived from known three-node traveltimes [case (2)] is good enough to be used as a substitute for that derived from known four-node traveltimes [case (1)]. Let us examine their accuracies using a homogeneous model with a velocity of 1000 m s^{-1} and with a cell size of 1 m × 1 m × 1 m. Consider in Fig. 2 a source location S_0 and assume that theoretical traveltimes at the solid circle points are known. We compute traveltimes at different E locations using the formulas in cases (1) and (2), respectively. Fig. 3(a) shows

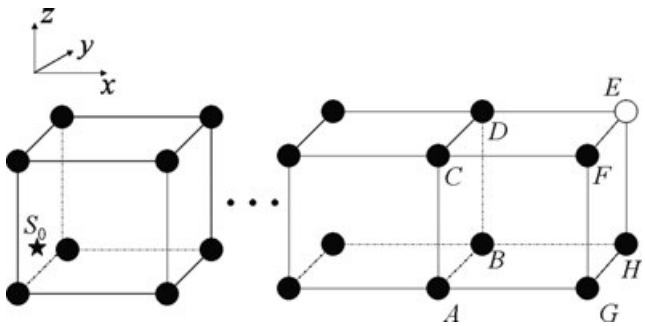

Figure 2. Model with homogeneous velocity of 1000 m s^{-1}. S_0 indicates the source. wave front traveltimes at the solid circle nodes have been known and traveltime at open circle node E is to be computed.

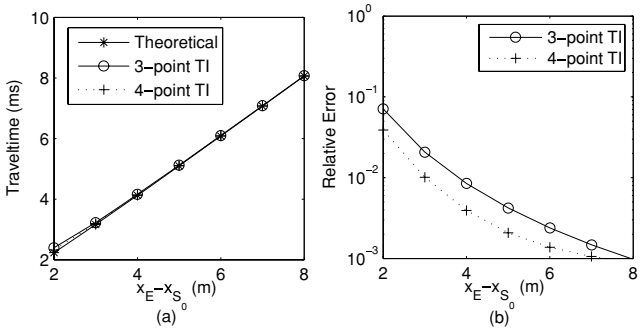

Figure 3. Accuracy comparison for the TI method in cases (1) and (2) at different E locations: (a) traveltimes; (b) relative error.

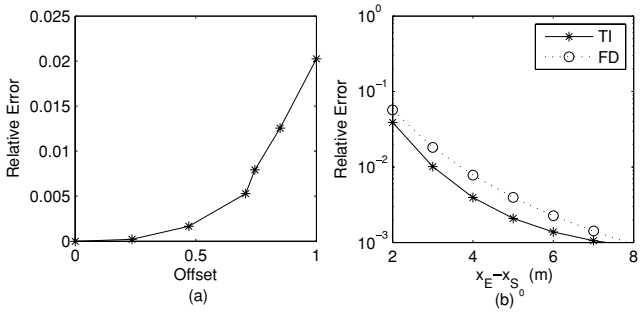

Figure 4. Accuracy comparison for TI method based on truncated approximation of Taylor series. (a) Approximation error for TI solutions with truncation. (b) Relative error with respect to the distance between the source and the point E.

the traveltime distribution for different E locations relative to a source point. Fig. 3(b) shows the corresponding relative errors in traveltimes versus the distance between S_0 and E. One can see that the formulas in case (1) always hold higher accuracy than the formulas in case (2) and should be used whenever known four-node traveltimes are available.

Next to demonstrate how accurate the approximation of eq. (3) to eq. (2) is, we set a series of S locations randomly on the left surface of a cell with different offsets away from the surface's centre. Then traveltimes at those positions are calculated by eqs (2) and (3). Fig. 4(a) shows the approximation error in traveltime using eq. (3) versus the offset. Here, the offset is defined as the distance between the point S and the surface centre divided by half the diagonal length of the surface and thus it is within a range of [0, 1]. The approximation error increases when the offset from the surface centre become larger. The numerical phenomenon is consistent with the expected behaviour dictated by a Taylor series expansion with respect to surface centre. Overall, the approximation error is less than 2 per cent and thus the feasibility of our approximation method is validated.

Furthermore, we calculate the traveltimes at different E locations for the model in Fig. 2 and compare them with the FD and the theoretical solutions (see Fig. 4b). The FD traveltimes are obtained by the solution of first-order FD of eikonal equation (traveltimes at D, F and G are used here). One can see that our method is much more accurate than the first-order FD method. Note that our method makes use of all the known grid nodes on the cell, while the FD method only uses partial of these.

It is noting that when a wave front discontinuity or shock evolves, it may be possible to mix unrelated information while performing the interpolation across a surface. One solution to solve this problem is to additionally calculate the traveltimes separately from each known grid node. Then the minimum of those calculated traveltimes from the cell surfaces and grid nodes will be selected as the wave front traveltime.

2.3 Wave front marching

Once a complex heterogeneous medium model is partitioned into a series of rectangular cells, we can use the FMM (Sethian 1999, 2001) and GMM (Kim 2002) to march the wave front outward from the source. Fig. 5 shows a 2-D wave front marching procedure. This process continuously selects a secondary source and updates the traveltimes around its neighbouring grid nodes (these grid nodes make up the wave front narrow band, see the shaded area in Fig. 5). The FMM expands the narrow band by selecting only one point with a minimum traveltime in the narrow band as a new source and readjusting outward neighbours. This treatment makes the FMM less efficient with the computational complexity of $O(N \log N)$, where N is the total number of grid nodes. As an improved variant of the FMM, the GMM expands its narrow band by locating a group of minima (when they are known) while maintaining causality and recomputing the traveltimes around their neighbours once at one time. The GMM has its complexity of $O(N)$ thus much faster than the FMM when N is large. We use the GMM combined with traveltime interpolation scheme given in Section 2.1.

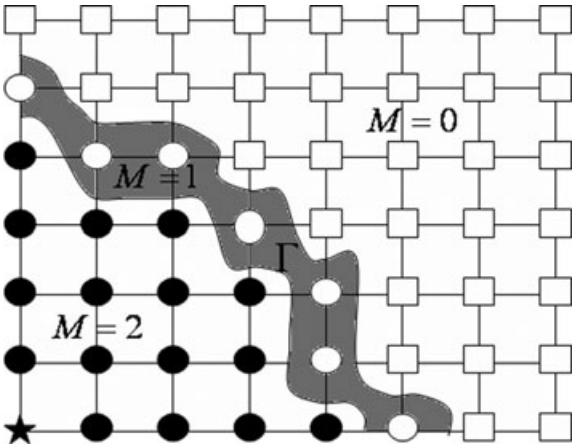

Figure 5. Wave front marching scheme in FMM and GMM. Given a source location denoted as a star and the nodes (solid circles) with known wave front traveltimes, we will determine wave front traveltimes at those nodes (open circles) distributed within a narrow shaded band and then march to compute traveltimes at the nodes denoted as squares.

Following Kim (2002), consider a narrow band Γ of a wave front (see the shaded area in Fig. 5) and define

$$\delta t_\Gamma = \min\{(\Delta x, \Delta y, \Delta z\}/(\sqrt{3} v_{\Gamma,\max}), \tag{13}$$

where $v_{\Gamma,\max} = \max\{v_{i,j,k} : \in \Gamma\}$, and i, j and k denote the grid node number in x, y and z directions, respectively. According to Kim (2002), if the difference of the traveltimes at two nearby nodes in Γ is less than δt_Γ, the propagation energy on the two nodes will not interact on each other. Hence, a group of nodes G in Γ can be selected as follows:

$$G = \{(i, j, k) \in \Gamma : t(i, j, k) \le t_{\Gamma,min} + \delta t_\Gamma\}, \tag{14}$$

where $t_{\Gamma,\min} = \min\{(i, j, k) \in \Gamma : t(i, j, k) \le t_{\Gamma,\min} + \delta t_\Gamma\}$.

Tag the nodes to be computed as $M = 0$, the nodes in narrow band as $M = 1$, and the nodes whose traveltimes are determined as $M = 2$ (see Fig. 5). Then, the GMM loop is carried out as

(1) Initialization
  (i) Assign a large number for the solutions of all nodes, e.g. $t_{i,j,k} = 10^5$;
  (ii) Set $M_{i,j,k} = 0$ for all nodes;
  (iii) On the box of $2 \times 2 \times 2$ cells with the point source at its centre,
    (a) Set $M_{i_0,j_0,k_0} = 2$ for the point source;
    (b) Set the solution at the point source as zero, for example, $t_{i_0,j_0,k_0} = 0$, and compute solutions at all other nodes with the traveltime interpolation-based equations;
    (c) Set $M_{i,j,k} = 1$ for the nodes computed, and move them into Γ.
(2) Marching forward
  (i) Set $t_{\Gamma,\min}$ to be the minimum t and $v_{\Gamma,\max}$ to be the maximum v in the Γ;
  (ii) Compute δt_Γ with eq. (12), and then set $t_{\Gamma,\min} = t_{\Gamma,\min} + \delta t_\Gamma$;
  (iii) For each node in Γ, if $t_{i,j,k} \le t_{\Gamma,\min}$ is satisfied:

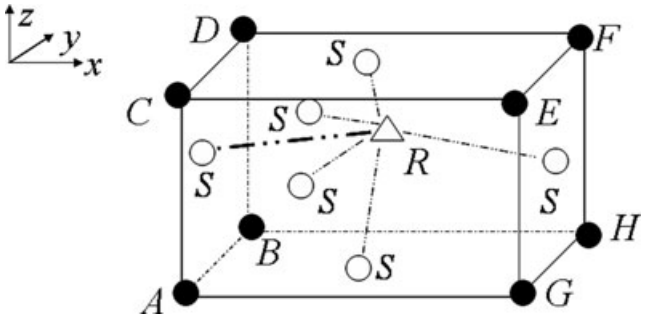

Figure 6. Ray tracing in a cell. With known wave front traveltimes at nodes (solid circles), candidate rays can be traced back from a receiver R (triangle) to points (open circles) on the surface of a cell, and a path (e.g. a thick dotted line) having minimum traveltime is selected as a ray.

(a) Update the neighbouring nodes (l, m, n) which satisfy $M_{l,m,n} = 1$ with traveltime interpolation-based equations. Otherwise, if $M_{l,m,n} = 0$, compute wave front traveltimes at the nodes (l, m, n) with the traveltime interpolation-based equations, set $M_{l,m,n} = 1$ and move them into Γ;

(b) Remove the node (i, j, k) out of Γ, and set $M_{i,j,k} = 2$;

(iv) if Γ is not empty, go to (i).

This completes the description of the wave front marching procedure used in our method.

2.4 Ray tracing

After the wave front traveltimes at all grid nodes of discrete media are computed, ray tracing can be conducted backward from receivers to sources. This involves in finding the intersection points of a ray path and each of the corresponding cell surfaces. Fig. 6 show how one can perform a ray tracing. A, B, C, D, E, F, G and H are the nodes in a cell and their wave front traveltimes are known. A receiver, denoted as R with its location of (x_R, y_R, z_R), can be in the cell or on one of the cell's surfaces. The ray tracing in this cell is to find the point S on the cell's surfaces so that the traveltime from source and through it to R is a minimum. The location of the point S on each surface of the cell and the corresponding traveltime through S to R can be calculated using eqs (1)–(6) with a substitution of R for E. Among those S points, the point with the minimum traveltime is chosen as the intersection point of the ray path from source to receiver R (see open circles in Fig. 3). The line connecting the intersection point and receiver R approximates the ray path in the cell (thick dotted line in Fig. 6). In summary, the ray tracing process is as follows:

(1) When one receiver is in one cell, we calculate the intersection point of a ray path with the surfaces of that cell. When one receiver is on the surface between n cells (n can equal to 2, 4 and 8, corresponding to the receiver is on the surface within the edge, on the edge, and on a grid node, respectively), we calculate the intersection point on each surface of n cells and then select the correct one among all those candidate points.

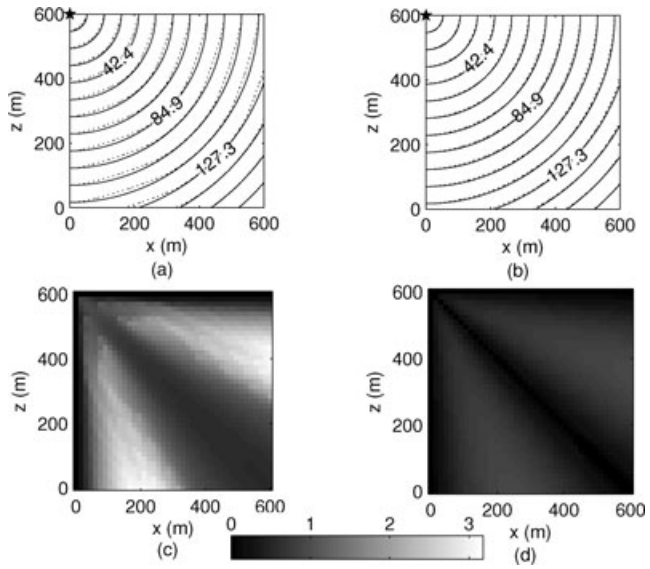

Figure 7. Wave front traveltime contours and absolute error distribution on the vertical slice ($y = 300$ m) of model 1. (a) Theoretical traveltimes (solid lines) and computed ones with the FD-GMM (dashed lines). (b) Theoretical traveltime (solid lines) and computed ones with the TI-GMM (dashed lines). (c) Absolute error of the FD-GMM. (d) Absolute error of the TI-GMM. Values labelled on contours represent their corresponding traveltimes in ms.

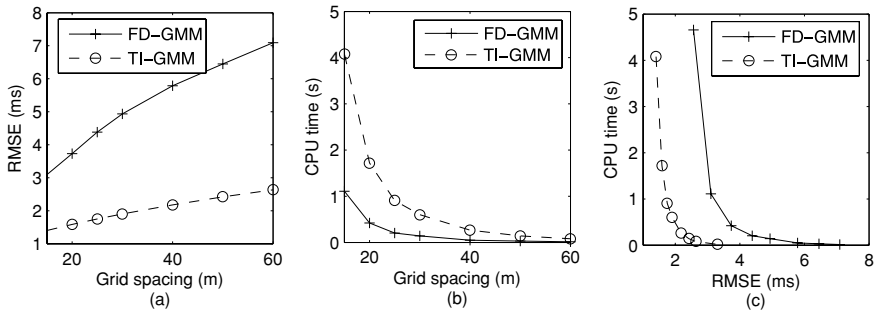

Figure 8. Accuracy of traveltime computation using the FD-GMM and the TI-GMM, respectively, versus cell size in model 1.

(2) We treat the intersection point found in step (1) as a new receiver and repeat (1) until an intersection point locates on the surface of the cell where the primary source is in it.

(3) Connecting the source, all intersection points and the receiver, we obtain the ray path between the source and the receiver.

3 NUMERICAL EXPERIMENTS

To illustrate the accuracy and efficiency of our algorithm (traveltime interpolation-based GMM, denoted as TI-GMM), we use three models: homogenous, vertically inhomogeneous and arbitrary media in the experiments. In the first two media, there are analytical solutions that allow us to examine the performance of our ray tracing technique in terms of wave front traveltimes and ray paths. For the forward part, the results from the second-order finite difference GMM (FD-GMM) is presented for comparisons. For the backward part, the SPM and the maximum gradient method with the second-order FD solver (FD-MG) are also implemented for comparisons.

To measure the algorithm accuracy, we use the root mean square error (RMSE) defined as

$$\mathrm{RMSE} = \sqrt{\frac{\sum_{i=0}^{N_x-1}\sum_{j=0}^{N_y-1}\sum_{k=0}^{N_z-1}(\hat{t}_{i,j,k}-t_{i,j,k})^2}{N_x N_y N_z}}, \tag{15}$$

where N_x, N_y and N_z are the grid number along each direction, respectively, $\hat{t}_{i,j,k}$ indicates the numerical solution and $t_{i,j,k}$ is the theoretical or reference value. The main programs were written in C++ and the numerical experiments were performed on a PC with an Intel core 2 Duo processor of 1.6 GHz and 1 GB RAM memory under Windows XP operation system, using Microsoft Visual Studio.net 2003.

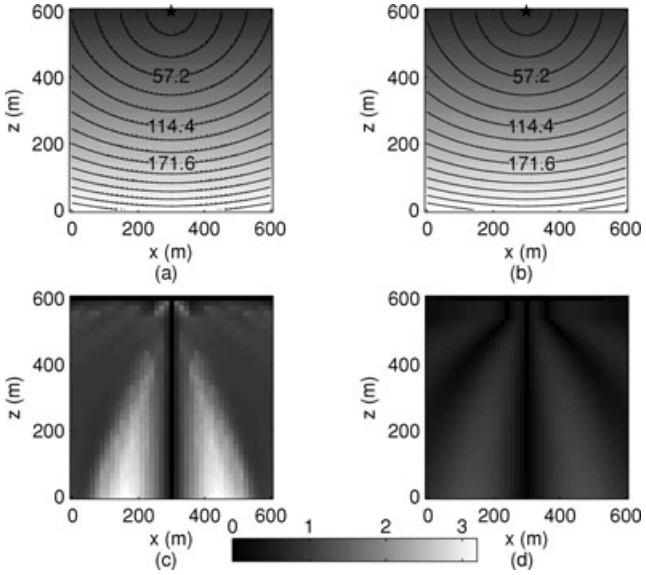

Figure 9. Wave front traveltime contours and absolute error distribution on the vertical slice ($y = 300$ m) of model 2. (a) Theoretical traveltimes (solid lines) and computed one with FD-GMM (dashed lines). (b) Theoretical traveltime (solid lines) and computed one with TI-GMM (dashed lines). (c) Absolute error of FD-GMM. (d) Absolute error of TI-GMM. Values labelled on contours represent their corresponding traveltimes in milliseconds.

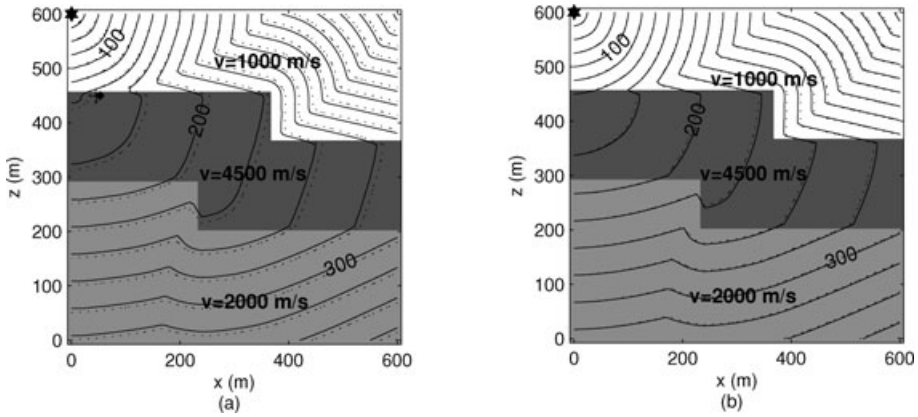

Figure 10. Vertical slices ($y = 0$ m) of contour traveltimes superposed on model 3. Source located at (0 m, 0 m, 600 m). (a) Wave fronts computed with the FD-GMM; (b) wave fronts computed with the TI-GMM. Solid lines indicate wave fronts computed with cell size of 7.5 m × 7.5 m × 7. 5 m; dashed lines indicate wave fronts computed with cell size of 15 m × 15 m × 1 5 m.

3.1 Wave front traveltimes

3.1.1 A homogeneous medium

In the first experiment, a simple 3-D homogeneous medium model (model 1) is used with its size of 600 m × 600 m × 60 0 m and a constant velocity of $v = 5000\ \mathrm{m\,s^{-1}}$. The model is discretized into 40 × 40 × 40 cells. Each cell has a size of 15 m × 15 m × 1 5 m. A point source is located at (300 m, 300 m, 300 m). Wave front traveltimes are computed using FD-GMM (Kim, 2002) and our TI-GMM. The FD-GMM has the RMSE of 2.56 ms, while our TI-GMM has only 0.98 ms.

Figs 7(a) and (b) are the vertical slices ($y = 300$ m) of wave front traveltimes computed with FD-GMM and TI-GMM, respectively, where solid lines indicate theoretical traveltime contours and dashed lines represent computed ones. Figs 7(c) and (d) are their corresponding absolute error distributions between theoretical traveltimes and the numerical solutions. The error of TI-GMM is much smaller than that of FD-GMM. The TI-GMM provides very accurate 3-D traveltime computation.

To make CPU time-accuracy (RMSE) comparison between TI-GMM and FD-GMM, we computed the wave front traveltimes of model 1 discretized with different grid spacings. Fig. 8(a) shows the accuracy behaviour of these two methods with the variation of the cell size in model 1. Clearly, the accuracy of our TI-GMM is much higher than the FD-GMM and becomes more predominant when the cell size

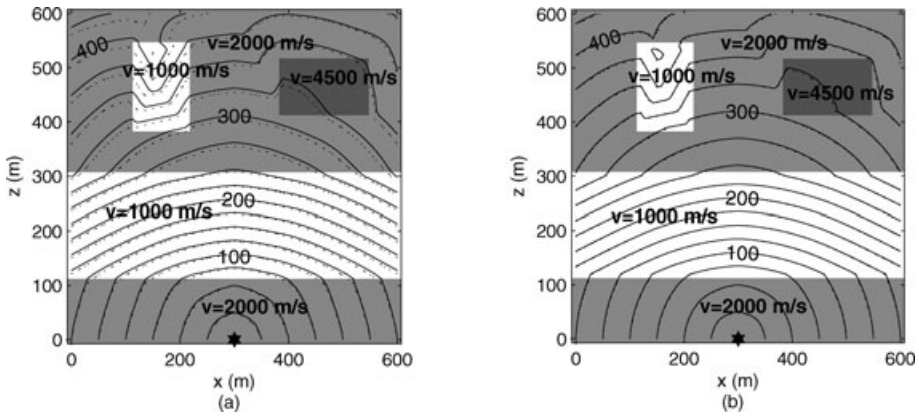

Figure 11. Vertical slices ($y = 300$ m) of contour traveltimes superposed on model 4. Source located at (0 m, 300 m, 0 m). (a) Wave fronts computed with the FD-GMM; (b) wave fronts computed with the TI-GMM. Line legends are the same as in Fig. 10.

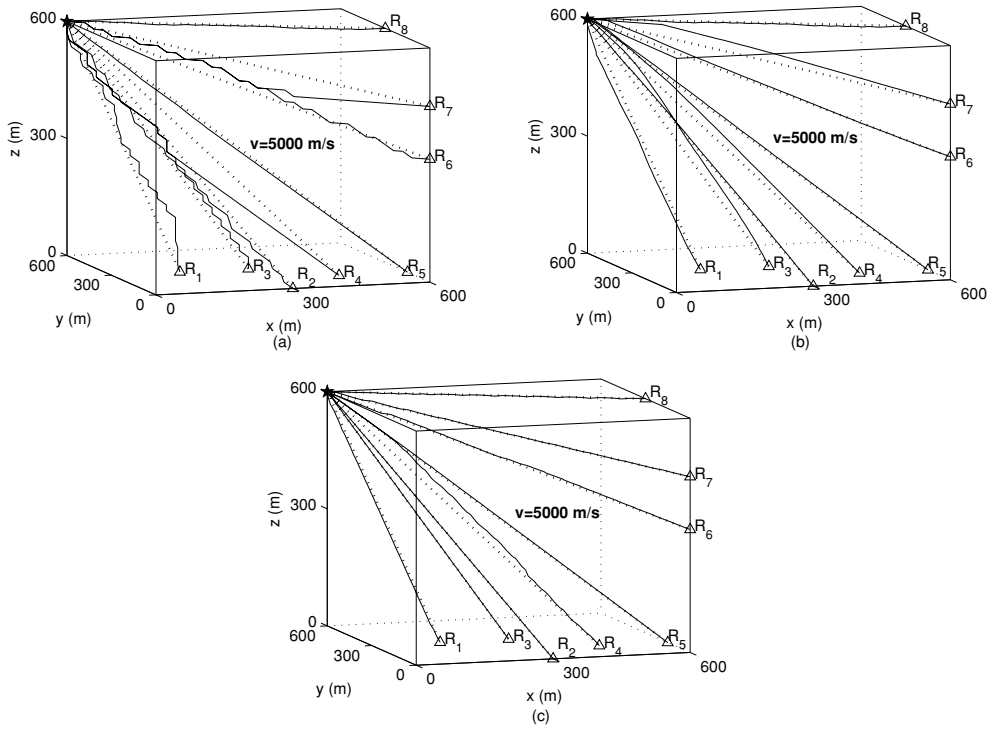

Figure 12. Ray paths in model 1. (a) Ray paths traced by the SPM; (b) ray paths traced by the FD-MG; (c) ray paths traced by the TI-GMM. Dashed lines indicate theoretical ray paths. S indicates sources and R indicate receivers (same as in Figs 14, 16 and 17).

increases. On the other hand, Fig. 8(b) depicts the CPU-time used in the two methods against the cell size. Our TI-GMM appears to take a longer CPU time in traveltime computation than the FD-GMM. This is because the TI requires the traveltimes from multisurfaces of each cell. However for the FD scheme to achieve same high-accuracy as our TI, one can see, referring to Fig. 8(a), that it has to use much smaller cell sizes in traveltime computation and thus actually requires more CPU-time. Fig. 8(c) shows this efficiency behaviour of the two methods against accuracy demand. It is clearly illustrated that our method can use a bigger cell size and has much less computation cost than FD-GMM without compromising accuracy of traveltime computation. This feature is very important in the application of traveltime tomography. From these experiment results, we can conclude that our TI-GMM holds superiority in both accuracy and efficiency to the FD-GMM.

3.1.2 A vertically inhomogeneous medium

In this experiment, we consider a 3-D vertically inhomogeneous medium model (model 2), that is, a velocity increasing linearly with depth $v = 1000 + 5z$ m s^{-1} over a computational domain of 600 m $\times$ 600 m $\times$ 600 m. For this constant velocity gradient model, the analytical calculation of traveltime from the source to any point position is available (Slawinski & Slawinski 1999). In the numerical experiment, we

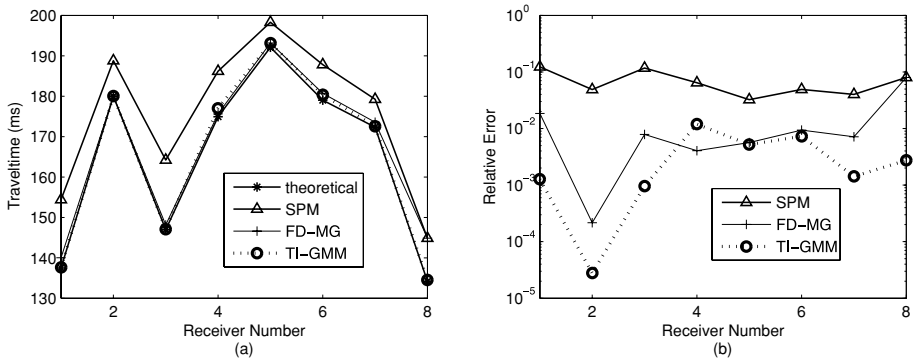

Figure 13. Comparison of traveltimes for ray paths in model 1 with analytical values. (a) Numerical and analytical solutions and (b) relative error distribution.

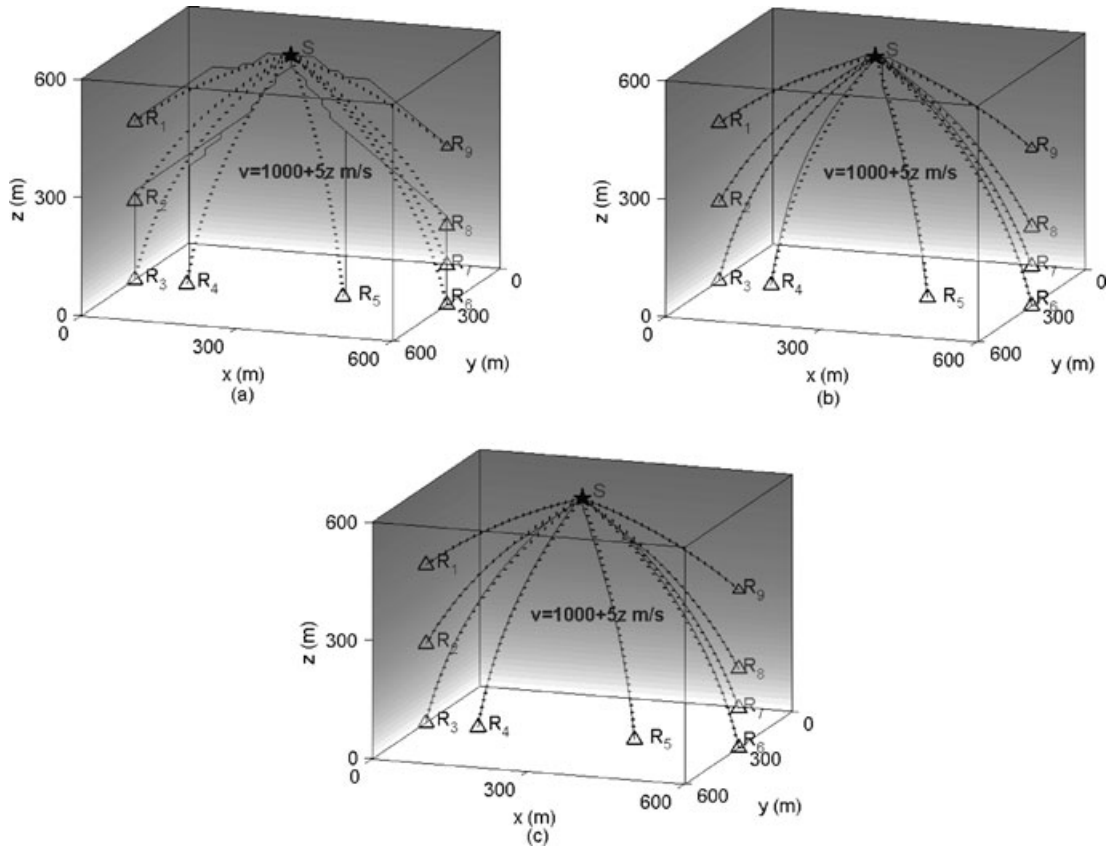

Figure 14. Ray paths in model 2. (a) Ray paths traced by the SPM; (b) ray paths traced by the FD-MG and (c) ray paths traced by the TI-GMM. Dashed lines indicate theoretical ray paths.

discretized the model into 40 × 40 × 40 cells. Each cell has a size of 15 m × 15 m × 1 5 m. A source point is located at (300 m, 300 m, 600 m).

Figs 9(a) and (b) are the vertical slices ($y = 300$ m) of wave front traveltimes computed with FD-GMM and TI-GMM, respectively, where solid lines indicate theoretical traveltime contours and dashed lines represent computed ones. Figs 9(c) and (d) are their corresponding absolute error distributions between theoretical traveltimes and the numerical solutions. Again, the results show that the TI-GMM is able to achieve very high accuracy as compared to the FD-GMM.

3.1.3 Arbitrary inhomogeneous media

Next we examine the traveltime computation in arbitrary media. Two models were used. A 3-D layered faultage model, labelled as model 3, shown in Fig. 10, has a size of 600 m × 600 m × 600 m. In this model, the upper layer has a velocity of 1000 m s^{-1}, the middle layer a velocity of 4500 m s^{-1} and the lower layer 2000 m s^{-1}. Another inhomogeneous model, labelled as model 4, consists of three layers of media with the velocity of 1000 m s^{-1} in the middle layer and 2000 m s^{-1} in both the upper and the lower layers, and the upper layer includes two local bodies with the velocity of 1000 and 4500 m s^{-1}, respectively (Fig. 11). The size of model 4 is also 600 m × 600 m × 60 0 m. These two models were subdivided into a series of uniform cells, with different sizes of 15 m × 15 m × 1 5 m and 7.5 m × 7.5 m × 7. 5 m, respectively. Figs 10 and 11 show the 2-D vertical slices of the contour wave front traveltimes superposed on these two complex heterogeneous models.

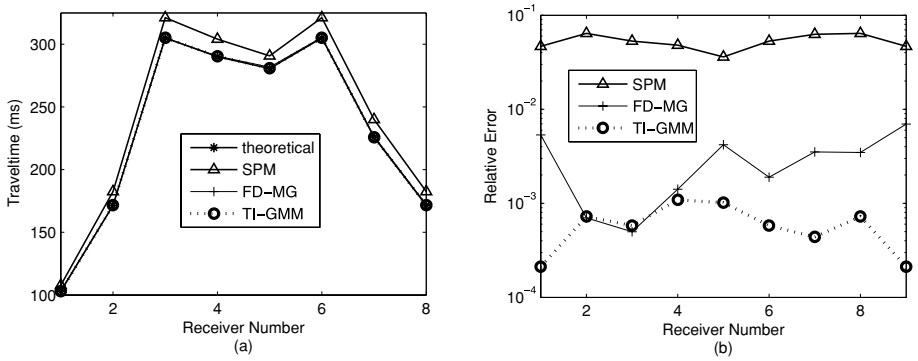

Figure 15. Comparison of traveltimes for ray paths in model 2 with analytical values. (a) Numerical and analytical solutions and (b) relative error distribution.

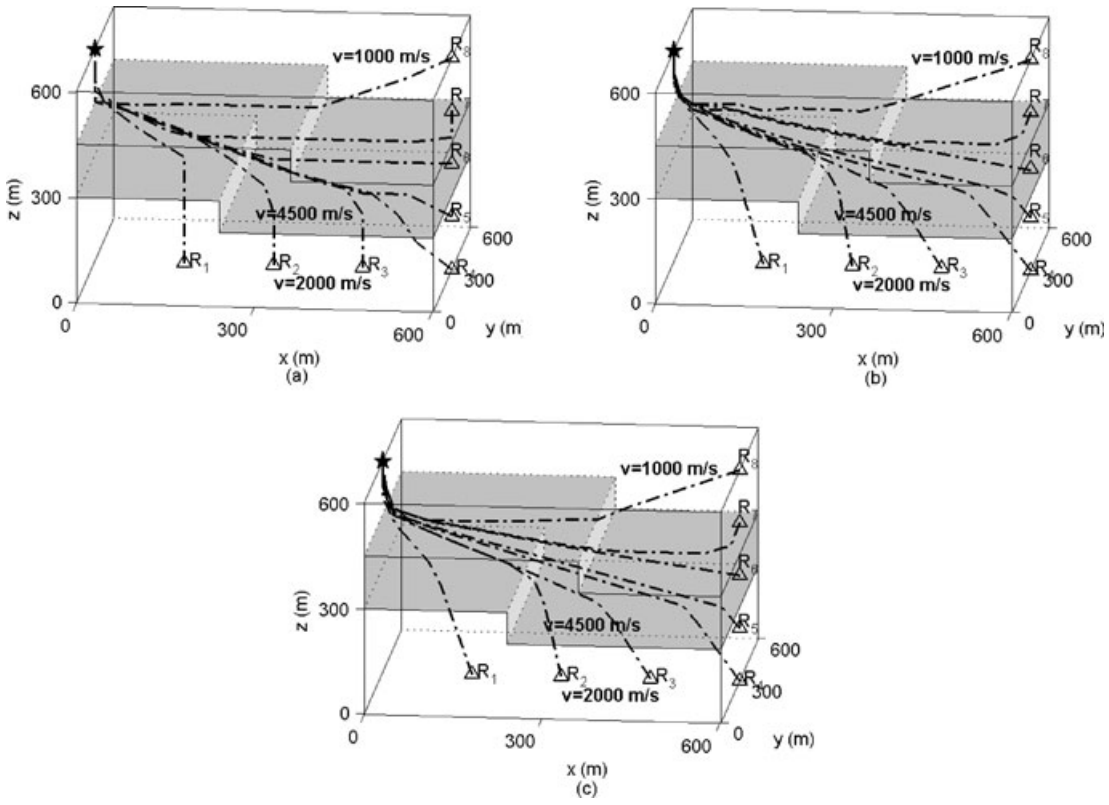

Figure 16. Ray paths in model 3. (a) Ray paths traced by the SPM; (b) ray paths traced by the FD-MG and (c) ray paths traced by the TI-GMM.

The wave front traveltimes in these two models were computed using FD-GMM and TI-GMM, with different cell sizes. Both methods show the correct physical characteristic of wave front propagation in the heterogeneous velocity models. One can see that the difference between the two sets of wave fronts with different cell sizes by the TI-GMM is smaller than that by the FD-GMM. This phenomenon shows that with bigger cells the TI-GMM method performs better than the FD-GMM, which is consistent with the conclusion from Fig. 8.

3.2 Ray paths

In this section, we examine ray tracing process using the SPM (Moser 1991), the maximum gradient method with second-order FD solver (FD-MG) and the proposed TI-GMM with above-mentioned models.

Fig. 12 depicts ray paths traced by the SPM, the FD-MG and the TI-GMM in model 1, with the uniform cell size of 15 m × 15 m × 1 5 m. Fig. 12(a) shows the ray paths traced by the SPM. The SPM joins all gridpoints that satisfy the least time principle thus the SPM ray paths are flexuous and are different from theoretical straight rays (similar numerical problem seen in Fischer and Lees 1993). Fig. 12(b) shows ray paths traced by the FD-MG. Our TI-GMM produces the most accurate ray paths (Fig. 12c) with the same cell size. Fig. 13 compares the theoretical ray path traveltimes from a source to different receivers along the corresponding rays traced by the SPM, the FD-MG and the TI-GMM, respectively. We can see that the SPM renders a seriously systematic larger values than theoretical ones; the FD-MG produces traveltime solutions much closer to the theoretical ones; and the TI-GMM gives the most accurate solutions.

For model 2, the ray paths traced by the SPM, the FD-MG and the TI-GMM are shown in Fig. 14 with the uniform cell size of 15 m × 15 m × 1 5 m. In this medium, the theoretical ray paths are calculated analytically (see the dashed lines in Fig. 14). The ray paths traced by the SPM in Fig. 14(a) are very different from the theoretical ones because of the big cell size. The FD-MG gives much more accurate ray paths which are closer to the theoretical ones (Fig. 14b). Our TI-GMM again accurately produces ray paths (Fig. 14c) using the same cell size. Fig. 15 compares the theoretical ray path traveltimes from a source to different receivers along the corresponding rays traced by using the SPM, the FD-MG and the TI-GMM, respectively. One we can see is that the proposed TI-GMM method produces traveltime solutions most accurately compared with the SPM and the FD-MG schemes.

For the arbitrary inhomogeneous models, that is, models 3 and 4, the ray paths found by the SPM, the FD-MG and the TI-GMM are shown in Figs 16 and 17 with the uniform cell size of 15 m × 15 m × 1 5 m. One can see that some ray paths obtained by the SPM are physically not reasonable. Ray paths traced by the FD-MG and the TI-GMM methods are close to each other. To tell the difference between the FD-MG and the TI-GMM methods, we also show Figs 18 and 19 to give comparison of traveltimes for ray paths in models 3 and 4 with reference values. Since the theoretical traveltime between each pair of source and receiver in these two models are not available, we take

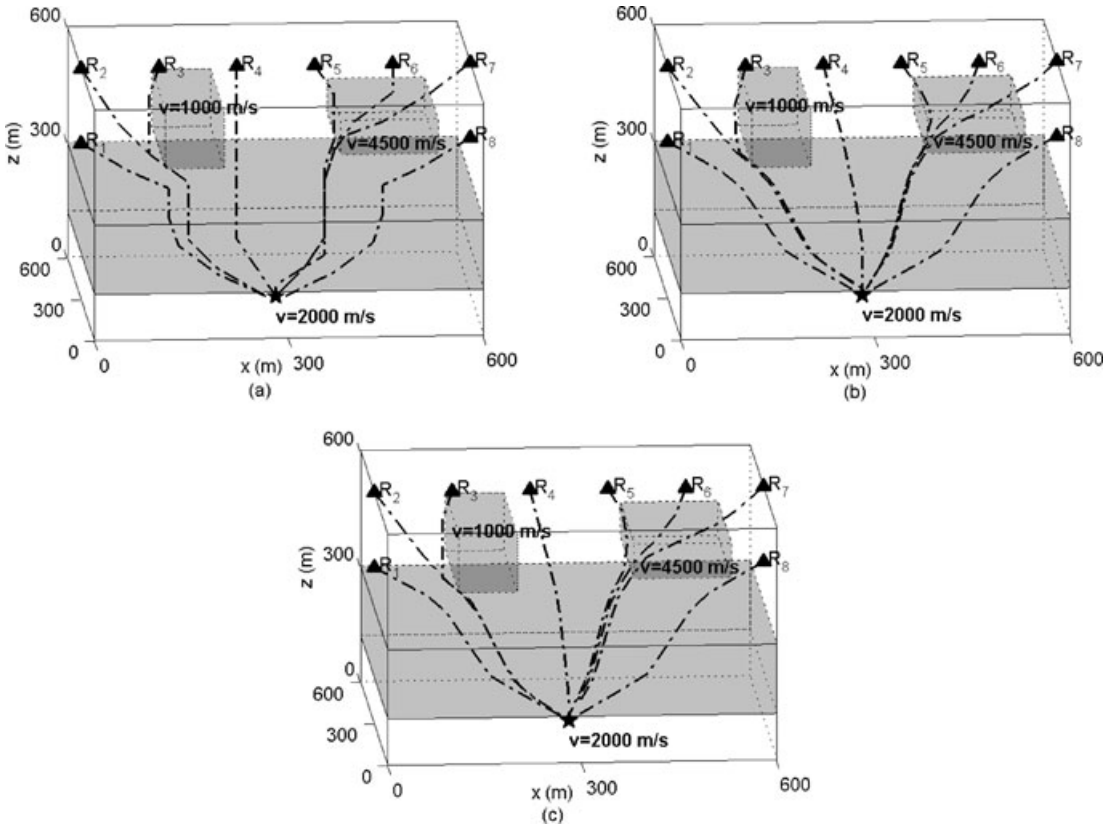

Figure 17. Ray paths in model 4. (a) Ray paths traced by the SPM; (b) ray paths traced by the FD-MG and (c) ray paths traced by the TI-GMM.

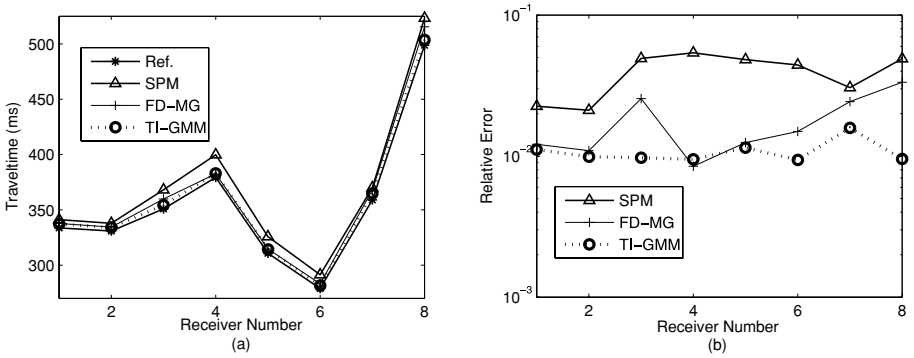

Figure 18. Comparison of traveltimes for ray paths in model 3 with reference values. (a) Numerical and reference solutions and (b) relative error distribution.

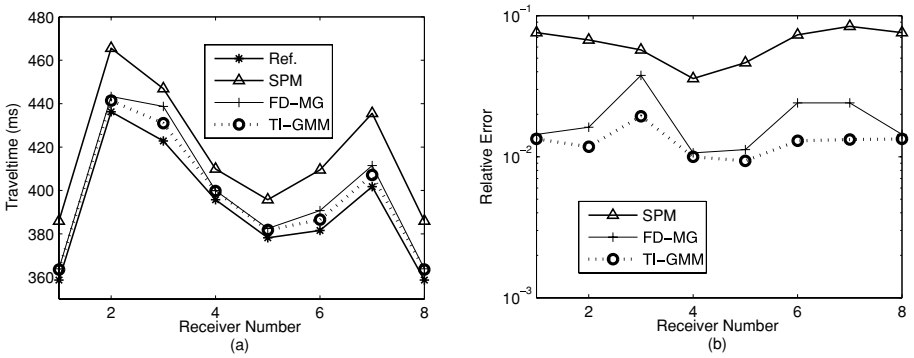

Figure 19. Comparison of traveltimes for ray paths in model 4 with reference values. (a) Numerical and reference solutions and (b) relative error distribution.

the traveltimes generated by the TI-GMM with a uniform cell size of 7.5 m $\times$ 7.5 m $\times$ 7. 5 m as reference values (the total number of the grid nodes is eight times the previous one). Then, the traveltimes calculated by the SPM, the FD-MG and the TI-GMM are compared with the reference values. It is obvious that the traveltimes calculated by the SPM are systematically larger than that by the FD-GMM and the TI-GMM for these complex models. Besides, these two experiments also depict that the TI-GMM method maintains the stablest accuracy level ($\approx$ or $\leq 10^{-2}$). Therefore, our TI-GMM has a far superiority to both the SPM and the FD-MG for ray tracing.

4 CONCLUSIONS

This paper has presented an algorithm for wave front traveltime calculation and ray tracing in 3-D complex heterogeneous isotropic media. For the forward part, the 2-D LTI wave front traveltime solver is extended for 3-D cases. The Taylor series with second-order accuracy is introduced to produce a closed-form expression for 3-D local traveltime calculation, based on a bilinear interpolation of known traveltimes over the grids in a cell. The combination of the efficient and stable GMM with our 3-D LTI traveltime solver renders a 3-D TI-GMM wave front calculation technique, which is different from the 2-D LTI wave front expansion scheme that may violate causality of wave propagation. For the backward part, the ray paths are traced by the same 3-D LTI solver, rather than the maximum gradient method in the traditional FMM/GMM-based algorithms. Through a series of tests, we observe that the proposed TI-GMM algorithm maintains very accurate computation of wave front traveltimes and consume much less CPU time as compared with the FD-GMM. From the accuracy comparison of ray paths computed with the SPM, the FD-MG and our TI-GMM ray tracing method, we can come to a conclusion that our TI-GMM ray tracing method is the stablest in terms of accuracy level, while can take transmission, refraction and diffraction into account in 3-D complex media and without difficulty of 'shadow zone effects' for any pair of source–receiver configurations.

ACKNOWLEDGMENTS

This work was supported by the National Natural Science Foundation of China (No. 41074077, 40774065). The author would like to thank the reviewers for their constructive comments and Jiefu Chen for his great help during our revision work.

REFERENCES

Asakawa, E. & Kawanaka, T., 1993. Seismic ray tracing using linear traveltime interpolation. *Geophys. Prospect.,* **41,** 99–112.

Bai, C., Greenhalgh, S. & Zhou, B., 2007. 3D ray tracing using a modified shortest-path method. *Geophysics,* **72,** T27–T36.

Cardarelli, E. & Cerreto, A., 2002. Ray tracing in elliptical anisotropic media using the linear traveltime interpolation (LTI) method applied to traveltime seismic tomography. *Geophys. Prospect.,* **50,** 55–72.

Cerveny, V., 2001. *Seismic Ray Theory,* pp. 53–73, Cambridge Univ. Press, New York.

Dijkstra, E.W., 1959. A note on two problems in connection with graphs. *Numer. Math.,* **1,** 269–271.

Fischer, R. & Lees, J.M., 1993. Shortest path ray tracing with sparse graphs. *Geophys.,* **58,** 987–996.

Giudici, M. & Gualteri, L., 1998. Application of revised ray tracing migration to imagine lateral variations of seismic fabric corresponding to different tectonic styles in the northern Apennines. *Tectonophysics,* **300,** 181–197.

Grunberg, M., Genaud, S. & Mongenet, C., 2002. Seismic ray-tracing and Earth mesh modeling on various parallel architectures, *J. Supercomput.,* 1–18.

Hturber, C.H. & Ellsworth, W.L., 1980. Rapid solution of ray tracing problems in heterogeneous media. *Bull. seism. Soc. Am.,* **70,** 1137–1148.

Huang, Y., Zhang, J., Liu, Q. H., 2010. Three-dimensional GPR ray tracing based on wavefront expansion with irregular cells, *IEEE Trans. Geosci. Remote Sens.,* in press.

Hysing, S.-A. & Turek, S., 2005. The eikonal eqution: numerical efficienty vs. algorithmic comlexity on quadrilateral grids. *Proc. Algoritmy,* **35,** 21–31.

Julian, B.R. & Gubbin, D., 1977. Three-dimensional seismic ray tracing. *J. Geophys.,* **43,** 95–114.

Kim, S., 2002. 3-D Eikonal solvers: first-arrival traveltimes. *Geophysics,* **67,** 1225–1231.

Klimes, L. & Kvasnicka, M., 1994. 3-D network ray tracing. *Geophys. J. Int.,* **116,** 726–738.

Li, X.G. & Ulrych, T.J., 1993. LTI formulation and application to curved wave fronts. *J. Seism. Explor.,* **2,** 239–246.

Majdanski, M., Grad, M. & Guterch, A., 2005. SUDETES 2003 working group: 2-D seismic tomographic and ray tracing modelling of the crustal structure across the sudetes mountains basing on SUDETES 2003 experiment data. *Tectonophysics,* **413,** 249–269.

Moser, T.J., 1991. Shortest path calculation of seismic rays. *Geophysics,* **56,** 59–67.

Nakanishi, I. & Yamaguchi, K., 1986. A numerical experiment on nonlinear image reconstruction from first-arrival times for a two-dimensional island arc structure. *J. Phys. Earth,* **34,** 195–201.

Podvin, P. & Lecomte, I., 1991. Finite difference computation of traveltimes in very contrasted velocity models: a massively parallel approach and its associated tools. *Geophys. J. Int.,* **105,** 271–284.

Qin, F., Luo, Y., Olsen, K.B, Cai, W. & Schuster, G.T., 1992. Finite-difference solution of the eikonal equation along expanding wave fronts. *Geophys.,* **57,** 478–487.

Rawlinson, N. & Sambridge, M., 2004. Wave front evolution in strongly heterogeneous layered media using the fast marching method. *Geophys. J. Int.,* **156,** 631–647.

Sethian, J.A. & Popovici, A.M., 1999. 3-D traveltime computation using the fast marching method. *Geophys.,* **64,** 516–523.

Sethian, J.A., 2001. Evolution, implementation, and application of level set and fast marching methods for advancing fronts. *J. Comput. Phys.,* **169,** 503–555.

Slawinski, R.A. & Slawinski, M.A., 1999. On raytracing in constant velocity-gradient media: calculus approach. *Can. J. Explor. Geophys.,* **35,** 24–27.

Spudich, P. & Neil Frazer, L., 1984. Use of ray theory to calculate high-frequency radiation from earthquake sources having spatially variable rupture velocity and stress drop, *Bull. seism. Soc. Am.,* **74,** 2061–2082.

Vasco, D.W. & Majer, E.L., 1993. Wavepath traveltime tomography. *Geophys. J. Int.,* **115,** 1055–1069.

Van Avendonk, H.J.A., Harding, A.J., Orcutt, J.A. & Holbrook, W.S., 2001. Hybrid shortest path and ray bending method for traveltime and raypath calculations. *Geophysics,* **66,** 648–653.

Vanelle, C. & Gajewski, D., 2002. Second-order interpolation of traveltimes. *Geophys. Prospect.,* **50,** 73–83.

Vidale, J.E., 1988. Finite-difference calculation of traveltimes. *Bull. seism. Soc. Am.,* **78,** 2062–2076.

Vidale, J.E., 1990. Finite-difference calculation of traveltimes in three dimensions. *Geophys.,* **55,** 521–526.

Wang, Y. & Houseman, G.A., 1995. Tomographic inversion of reflection seismic amplitude data for velocity variation. *Geophys. J. Int.,* **123,** 355–372.

Xiong, T., Zhang, M., Zhang, Y.T. & Shu, C.W., 2010. Fast sweeping fifth order WENO scheme for static Hamilton-Jacobi Equations with accurate boundary treatment. *J. Sci. Comput.,* **74,** 603–627.

Zhang, J., Chen, S. & Xu, C., 2004. A method of shortest path raytracing with dynamic networks. *Chin. J. Geophys.,* **47,** 899–904.

Zhao, H., 2004. A fast sweeping method for eikonal equations. *Math. Comput.,* **74,** 603–627.

Zhao, A., Zhang, Z. & Peng, S., 2004. Minimum travel-time tree algorithm for seismic ray tracing: improvement in efficiency. *J. geophys. Eng.,* **1,** 245–251.

Zhou, Z., Zhang, S. & Chen, L., 2004. Seismic ray-tracing calculation based on parabolic travel-time interpolation. *Cent. South Univ. Tech.,* **11,** 199–205.